PAPER

Experimental investigation on enhancement in pure axial deformation of soft pneumatic actuator (SPA) with cap ring reinforcement

To cite this article: Vishal Mehta *et al* 2024 *Eng. Res. Express* **6** 035512

Engineering Research Express

PAPER

Experimental investigation on enhancement in pure axial deformation of soft pneumatic actuator (SPA) with cap ring reinforcement

RECEIVED
1 June 2024

REVISED
26 June 2024

ACCEPTED FOR PUBLICATION
4 July 2024

PUBLISHED
16 July 2024

Vishal Mehta[1], **Mihir Chauhan**[1,2], **Harshal A Sanghvi**[3], **Erik D Engeberg**[2,4], **Javad Hashemi**[2] and **Abhijit Pandya**[3]

[1] Mechanical Engineering Department, Institute of Technology, Nirma University, Ahmedabad, Gujarat, India
[2] Department of Ocean and Mechanical Engineering, College of Engineering and Computer Science, Florida Atlantic University, Boca Raton, United States of America
[3] Department of Electrical Engineering and Computer Science, College of Engineering and Computer Science, Florida Atlantic University, Boca Raton, United States of America
[4] Center for Complex Systems and Brain Dynamics, College of Engineering and Computer Science, Florida Atlantic University, Boca Raton, United States of America

E-mail: mihir.chauhan@nirmauni.ac.in

Keywords: pure axial deformation, reinforcement, soft pneumatic actuator, soft robotics, bio-inspired soft-robots, liquid silicone rubber

Abstract

Bio-inspired soft-robots are nowadays found their place in many applications due to its flexibility, compliance and adaptivity to unstructured environment. The main intricate part of such bio-inspired soft robots are soft pneumatic actuators (SPA) which replicate or mimic the limbs and muscles. The soft actuators are pneumatically actuated and provide bending motion in most cases. However, many engineering and medical applications need axially expanding soft pneumatic actuators to deal with delicate objects. Various studies have put forward designs for SPA with axial deformation, but the majority of them have limited axial deformation, constraining motion and less overall efficacy which limit the scope of utilization. The common practice to enhance the axial deformation of SPA is by incorporating directionally customized reinforcement using fibres or by other means like yarns, fabrics, etc These types of reinforcements are generally embedded to SPA during fabrication and may not have capability for any correction or modification later on hence lack the customization. This paper presents a novel method of radial reinforcement for the enhancement of axial deformation of SPAs with provision of customization. The present study aims to enhance and/or customize the axial deformation of SPA by incorporating external and detachable reinforcement in the form of annulus shaped cap ring. The investigation encompasses the design and attachment of four distinct cap ring geometries to SPA at different locations. Experimental results affirm that cap ring reinforcement bolster the radial stiffness, curbing lateral deformation while permitting axial deformation of soft pneumatic actuators. Out of 64 distinct configurations, the one with full reinforcement, featuring four cap rings of maximum size, yields a remarkable 169% increase in pure axial deformation compared to unreinforced cases. It is also observed that by varying the number and placement locations of cap rings the pure axial deformation can be customized. This novel insight not only propels soft pneumatic actuation technology but also heralds prospects for highly agile and versatile robotic systems which can be used in medical, prosthetics, pharmaceutical and other industries.

Abbreviations and nomenclature

Abbreviations

SPA	Soft Pneumatic Actuator
LSR	Liquid Silicone Rubber
PLA	Polylactic acid

Nomenclature

θ_E	Effective arc angle
CR40	Cap ring with effective arc angle of 40°
CR60	Cap ring with effective arc angle of 60°
CR80	Cap ring with effective arc angle of 80°
CR100	Cap ring with effective arc angle of 100°
α_a	Axial dimension of deflated SPA
α_l	Lateral dimension of deflated SPA
β_a	Axial dimension of Inflated SPA
β_l	Lateral dimension of Inflated SPA
ε_a	Axial deformation ($\beta_a - \alpha_a$)
ε_l	Lateral deformation ($\beta_l - \alpha_l$)
λ	Ratio of axial deformation (ε_a) to lateral deformation (ε_l)
C	Configuration
D/XXXX	Configuration label

1. Introduction

Soft Pneumatic Actuators (SPAs) have emerged as a promising technology in the field of robotics and bioengineering, owing to their inherent compliance, lightweight nature, and ability to mimic the movement and dexterity of biological systems. SPAs are typically composed of elastomeric materials [1, 2] and rely on the inflation and deflation using air or other fluid to achieve motion. The recent development of SPAs for soft robotics majorly focusing on materials, construction, modelling, control systems and sensors [3].

Currently, many applications are embracing SPAs. In recent research [4], a soft robotic hand exoskeleton has been introduced that featuring five individually actuated digits, aiding individuals in piano play. They employed integrated tactile sensors alongside machine learning algorithms to differentiate accurate renditions of a song from incorrect ones. In a similar vein, researchers [5] proposed a soft pneumatic robotic digit comprising pneumatic bellows actuators, mimicking biological joints. Their study focused on achieving specific finger movements. A ground breaking design [6] has been detailed for a flexible robotic hand, employing pliable actuators capable of adapting to diverse grasping requirements. Another innovative contribution comes from the study [7], of a universal soft pneumatic gripper encompassing four bending actuators and a flexible wrist. A soft robot hand with fingertip haptic feedback [8] has been proposed for teleoperation to perform complex tasks and ensure safe and friendly human-machine interaction. This robotic hand can perform finger flexion/extension and abduction/adduction motions. In the realm of physical human-robot interaction, [9] air-filled materials were utilized to investigate vertical and horizontal force estimation. Inspired by the anatomical structure of octopus arms, a prototype robot arm [10] has been introduced composed of soft actuators, enabling fundamental octopus-like movements such as elongation, shortening, and bending. In the domain of adaptable stiffness, a novel soft robot arm design [11] has been introduced, capable of independently adjusting stiffness irrespective of spatial positioning. Study [12] has been conducted for the contribution to the field with a silicone-based climbing robot that emulates the locomotion of an octopus. Due to their extensive range of potential applications, researchers have shown a growing interest in SPAs. Several researchers have put forth various design and manufacturing methods to advance this field. A novel soft fluidic elastomer actuator [13] has been introduced that achieves three degrees of freedom in omnidirectional movement: bending, elongation, and contraction. Research [14] has been focused on the kinematics methodology of SPAs, offering a comprehensive approach to modelling these actuators while considering diverse design parameters. In a unique direction, work [15] has been explored for a robot's design that operates without external power sources like electricity or air compressors. This robot relies solely on the temperature gradient between the ground and the air to facilitate its movement on the ground. A study [16] has been presented on the impact of geometrical shapes on the axial deformation of soft pneumatic actuators, shedding light on the role of design in actuator performance. This type of axially deforming SPA is incorporated in an amphibious mobile robot to generate a rowing action underwater [17].

Challenges [18] have been addressed for directional and operational pressure by developing a pneumatic soft actuator encased in silicone rubber, referred to as a sponge core soft rubber actuator. An innovative design involving 3D printable robotic ball joints [19] has been contributed capable of creating adjustable stiffness

linkages between robot links through pneumatic actuation. This ball joint can swiftly lock the inner ball's position and orientation within the socket using pressurized air with its soft pneumatic elastomer actuator. In a biomimetic approach, a new design [20] has been discussed in the form of pneumatic single-channel and double-channel actuators inspired by the expansion and contraction of a worm's somites. These actuators offer multi-movement capabilities and high environmental adaptability. Fluid-powered fibre-reinforced actuators [21] have been devised, mirroring the intricate movements of the index finger and thumb. Numerous researchers [22–35] have made significant contributions in various areas, showcasing their remarkable work.

Upon reviewing existing literature, it is understood that SPAs have established their significance across numerous practical applications, owing to the advantages they bring forth [36]. Nevertheless, certain challenges [36] hinder the seamless utilization of SPAs within specific applications. Among these challenges, a primary concern involves attaining the intended deformation patterns to achieve the desired range of motion. Furthermore, the confined axial deformation capacity poses limitations on the overall functionality in some practical scenario. To address these issues, numerous researchers have endeavoured to enhance the desired deformation and motion characteristics of SPAs by implementing diverse reinforcement strategies.

Coils [37] have been incorporated into the soft actuator while molding to amplify its bending deformation capabilities. An anisotropic layer [38] has been introduced within conventional Dielectric Elastomer Actuators to interlink bending and twisting deformations, optimizing the fibre spacing and orientation within this layer. An innovative circular pressure chamber geometry with dense fibre-based reinforcement [39] has been proposed to enhance actuator performance. A solution [40] has been presented by involving chamber reinforcement to mitigate ballooning effects and ensure uniform bending in SPAs. A novel three-air-chambered, fibre-reinforced soft actuator, specifically designed [41] to enhance gripping in wearable hand rehabilitation devices. A fibre-reinforced dielectric elastomer tension actuator [42] has been extensively examined under various loading conditions. Nguyen *et al* [43] have introduced a 3-chambered elastomeric actuator fortified with fibres and stretch sensors. Researchers [44] have innovated a soft actuator featuring a molded wooden chamber and fibre reinforcement, tailored for gentle gripping applications. A separate study [45] has been meticulously done for determining optimal fibre orientations for each constant curvature (CC) segment, contributing to the design of bending actuators. Investigation [46] has been carried out for the constricting behaviour of contracting fibre-reinforced elastomeric enclosure actuators arranged in a spiral configuration around cylindrical object. The modelling and fabrication of soft actuators [47] has been presented based on fibre-reinforced elastomeric enclosures, particularly focusing on a cylindrical actuator enveloped by a double helical fibre arrangement. A novel fibre winding technique [48] has been introduced for tendon actuators, enhancing both bending efficiency and output force. Inspired by hydraulic joints in spider legs, a study [49] has been proposed for a flexible joint actuator reinforced with fibres, offering advantageous rotational capabilities.

The analysis of existing literature underscores the positive impact of incorporating fibre reinforcement on the deformation characteristics of SPAs. Nevertheless, the application of fibre reinforcement demands specialized expertise, as it must be precisely administered to impart the desired stiffness and deformation direction to the SPA. This process necessitates accurate implementation during the molding stage, leaving limited room for subsequent adjustments. Furthermore, the improvement in axial deformation achieved through fibre reinforcement is comparatively modest in comparison to the gains observed in bending deformation. To unlock broader potential applications and elevate overall performance, there arises a need for advancing the pure axial deformation capabilities of SPAs through innovative forms of external reinforcement. This approach not only streamlines the SPA design but also offers ease of implementation, replacement, and modification to achieve the desired deformation outcomes.

The present study aims to address an experimental investigation on the enhancement in pure axial deformation of soft pneumatic actuators with externally provided annulus shaped cap ring reinforcement. The research will involve conducting deformation tests on actuators with and without the cap ring reinforcement, measuring their axial and lateral deformation under pneumatic pressure with varied number of cap rings and the varied placement of cap rings. Furthermore, a geometrical parametric analysis will be performed to determine the suitable cap ring configuration that maximizes the actuator's pure axial deformation. The nuanced results from the 64 different SPA configurations that we tested show high capability for customizable actuator applications. As soft robotic design principles are still not a fully mature science, there is uncertainty in the SPA performance characteristics after fabrication. These results show potential for controlling axial and lateral deformation to compensate for uncertainty in the design process. Furthermore, our multifaceted data show that one actuator could be used for multiple applications with simple modifications to the location, size, and number of rings utilized. This could be profoundly useful in numerous areas ranging from tooling operations for industrial robots to minimally invasive surgical procedures.

The second section of this paper describes the design of SPA and cap rings with their variance and also discuss the fabrication process. The details of experimental set up and design of experiment is discussed in third

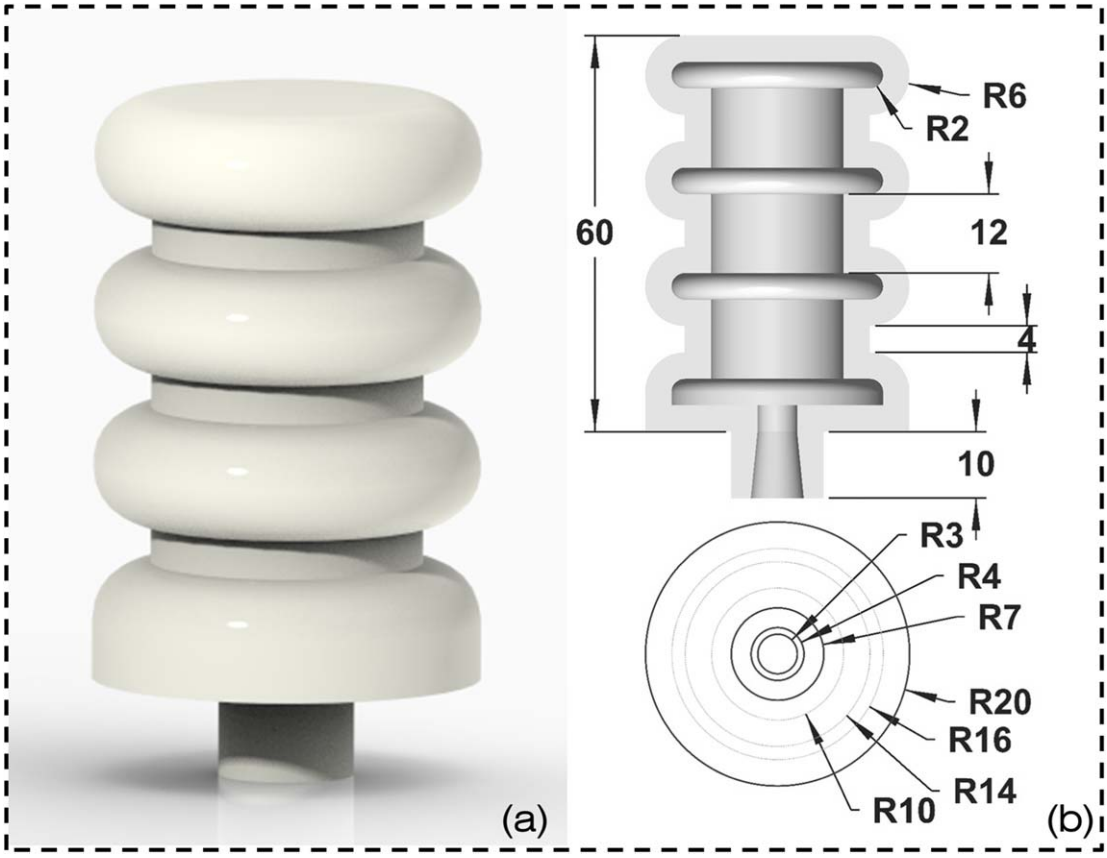

Figure 1. Design of SPA (a) 3D model of SPA, (b) detail dimensions and cross section view (All dimensions are in mm).

section. The experimental observations are also listed in this section. In section four the results are plotted and discussed. Useful conclusions are drawn and discussed in the last section with possibility of future extension of the work.

2. Materials and methods

During operation, SPA undergoes different kinds of deformation like bending, axial or lateral based on the application. The pattern of deformation can be achieved through systematic geometrical design of SPA.

2.1. Design of SPA

In the previous study [16] it is observed that internal and external geometrical shape of the air chambers significantly affect the deformation pattern and magnitude. The study [16] also reveals that the geometrical design of SPA as shown in figure 1(a) is the most promising shape to achieve the axial deformation of SPA. The structure comprises four axially arranged identical segments, shaped like buttons, with a capsule-shaped cross-section and spaced by cylindrical segments as illustrated in figure 1(b). The outermost radius of the button shaped segment is 20 mm while the inner radius is 16 mm, leads to the material thickness of 4 mm. The radius of curvature for button shaped segment is in accordance with the thickness of the material i.e., 6 mm for outer profile and 2 mm for inner profile and hence the height of the cavity inside the button shaped segment is 4 mm. The inner and outer radii of cylindrical shaped segments are 10 mm and 14 mm respectively while the height of this segment is kept as 4 mm. These dimensions are decided considering the manufacturing feasibility of SPA for experimentation.

The topmost button shaped segment is closed from the top while the bottom most button shaped segment is provided with an extended hollow cylindrical segment with outer radius of 7 mm while the inside hole is designed as convergent conical nozzle with major radius of 4 mm and minor radius of 3 mm. The convergent hole is specifically designed to attach the connector for the concentrated and directed air in-flow.

For the present study, where the major objective is to achieve maximum possible axial deformation, the materials should be flexible enough to provide large deformation for the applied pressure load. On the other hand, it should also provide sufficient strength to withstand the internal pressure load as well as external load

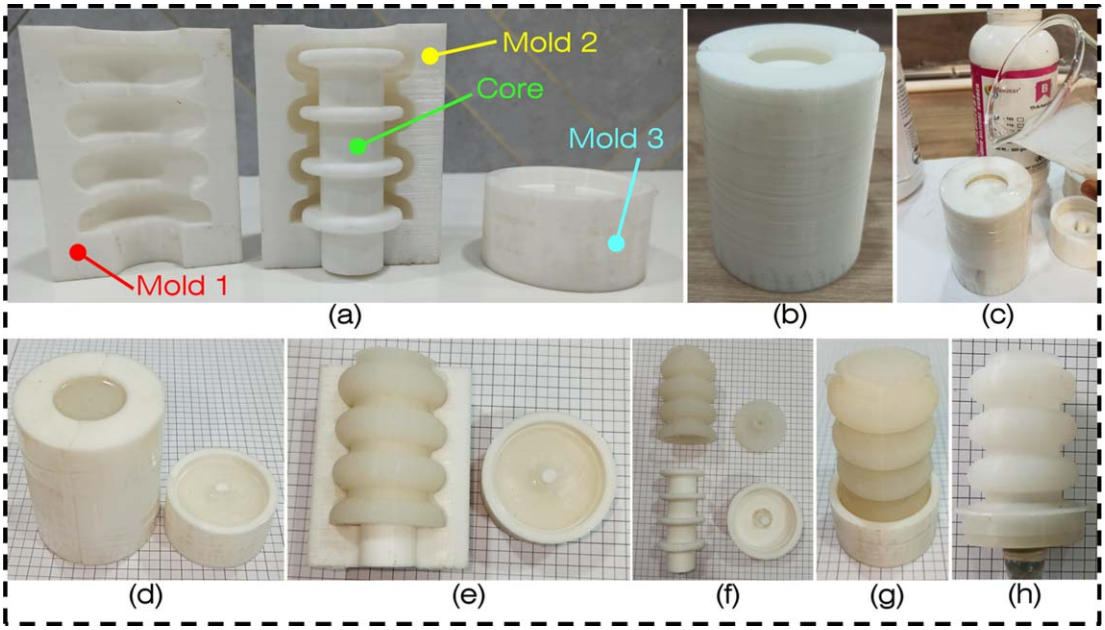

Figure 2. Fabrication of SPA (a) 3D printed molds, (b) mold assembly, (c) pouring LSR into the mold assembly, (d) curing time, (e) & (f) un-molding the SPA in two parts, (g) stage 2 curing, (h) final SPA. (The grid spacing on graph is 5 mm).

Table 1. Material properties of liquid silicon rubber (LSR) used in SPA [50].

Material	SILOCZEST LSR-115
Shore Hardness	15 A
Viscosity	3600 ± 1000 cps
Density	1.11 gm cm^{-3}
Pot life	20–30 min
Cure Time	5–8 h
Tensile strength	3.82 MPa

when put into operation. As per the manufacturer's catalogue, the SILOCZEST LSR-115 [50] material is the most appropriate LSR with the properties listed in table 1. It has shore hardness of 15 A which provides enough strength to withstand the internal pressure and also flexible enough to exhibit the large deformation. In addition, there is no requirement of degassing before pouring, during 20 to 30 min of pot life, and it has 5–8 h of reasonable cure time.

The SPA is fabricated in two stage molding process. Three molds and a core are 3D printed (Creality Ender-3 MAX 3D printer) using Polylactic acid (PLA) material with 100% filling (figure 2(a)). In stage 1, Mold 1 and Mold 2 are assembled keeping core within and fixed with an adhesive tape for the fitment (figure 2(b)). The open joints are applied with temporary glue to prevent the leakage of LSR. The LSR is prepared by mixing part A and part B in 1:1 proportion by volume and stirring it firmly until the homogeneous mixture is prepared. The prepared LSR is kept for approximately 5 min for degassing it naturally and then poured into the mold assembly (Mold 1 and Mold 2) as well as in mold 3 (figure 2(c)). The filled mold is allowed to rest for 7 to 8 h for curing (figure 2(d)). After curing the mold assembly is detached and the semi-finished SPA is un-molded and core is also removed (figures 2(e) and (f)). In stage 2, a thin layer of LSR is applied on already cured part of mold 3 and the upper part of actuators is placed vertically over it (figure 2(g)). After curing time, the mold 3 is detached and the complete SPA is ready for the experiments (figure 2(h)).

2.2. Design of reinforcement cap rings

The cap ring is designed in the form of thin annulus with uniform thickness of 1 mm, inner radius and outer radius of 20 mm and 21 mm respectively as shown in figure 3(a). The inner radius of the cap ring is decided such that the ring can be fit over the button shaped segment of the SPA externally. The height of the ring is decided based on the ring curvature angles. For the present study, four different effective arc angles are considered i.e., 40°, 60°, 80° and 100° as shown in figure 3(b) and accordingly four different cap rings are designed and

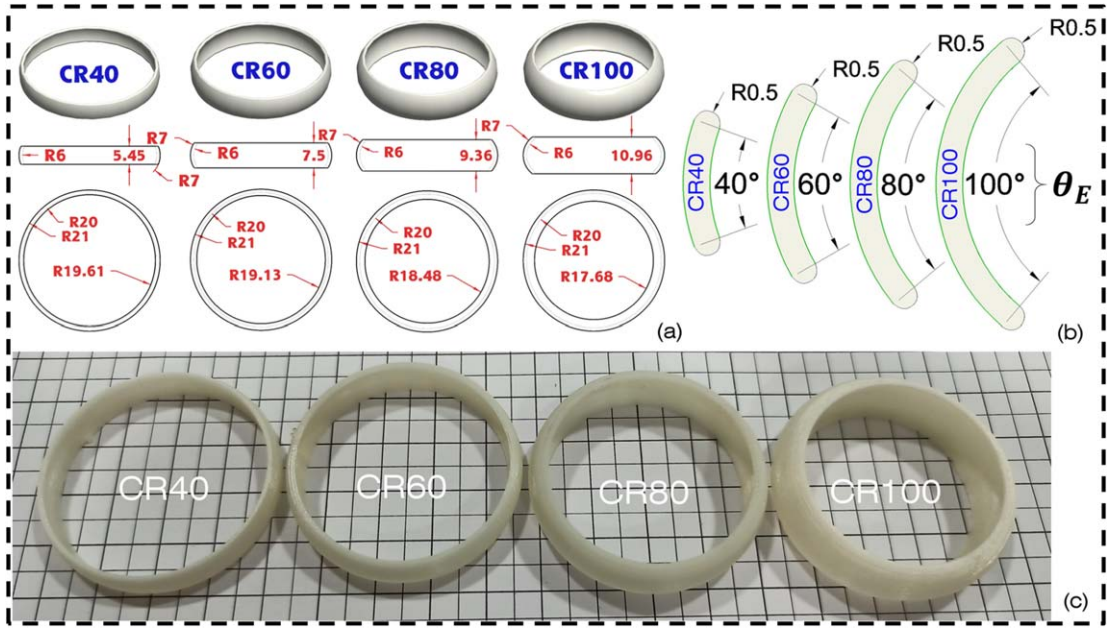

Figure 3. Cap ring with different effective arc angle (θ_E), (a) Solid models and drawings of cap rings, (b)Effective arc angle of cap ring (c) Actual images of 3D printed cap rings (All dimensions are in mm).

fabricated namely CR40, CR60, CR80 and CR100 with height of 5.45 mm, 7.5 mm, 9.36 mm and 10.96 mm respectively.

It is experimentally observed that the height of the ring with effective arc angle less than 40° becomes too small and hence it may not provide proper surface area for reinforcement and hence not consider in the present study. On the other hand, the cap ring with effective arc angle more than 100° has larger height that covers more surface area for reinforcement and may restrict the axial deformation. Due to these reasons the arc angle variations are considered within 40° to 100°. The cap rings are attached on the SPA externally at the button shaped region as shown figure 4 such that the central bisecting horizontal plane of button shaped segment and that of cap ring align to each other. The internal diameter of the cap rings is so selected that it fits firmly on the external surface without any aid of adhesive. Here, it is to note that there is total four segments over which the cap ring can be reinforced. Out of four, the bottom most button shaped segment has a bit different external profile as seen in figure 4. For the bottom most segment, the half segment of the designed cap ring is used for the reinforcement such that it matches the external profile of the button shaped segment.

2.3. Experimental investigation

To study the effect of cap ring reinforcement on the pure axial deformation of SPA the experimental set up is prepared as shown in figure 5. The major components are connectors (Brand SHOPEE, Universal Fit type, 13 mm diameter), digital air pump (MI portable electric air compressor, pressure range 20–995 kPa), ruler and graph papers (figure 5(a)). The SPA is connected to air pump using connectors for inflation (figure 5(d)).

It is considered that the size of cap ring, number of cap rings and placement (location) of cap rings plays important role and affect the pure axial deformation of SPA. Experiments are designed considering four different sizes of cap rings and four different locations of cap ring fittings. For ease of record keeping each experiment is designated by a label in the format like D/XXXX, where D represent the value of cap ring effective arc angle i.e., 40°, 60°, 80° and 100°, while XXXX stands for binary representations that shows number and location of cap ring. Each X corresponds to the one button shaped segment from top to bottom and assumed value 1 or 0 showing the presence or absence of cap ring respectively on that segment (figure 6). As there are four segments available for reinforcement, total of $2^4 = 16$ different configurations are possible for each of the cap ring arc angle as listed in table 2. Hence all together 64 configurations are experimented to check the effect of cap ring reinforcement on axial deformation of SPA. It is important to note that all these configuration cases are experimented using the single SPA to avoid the error arises due to manufacturing or material properties and hence it maintains the consistency and uniformity in all the experiments.

During the experiments, initially the deflated SPA without any cap ring attachment is measured for its axial dimension (α_a) and lateral dimensions (α_l) and recorded as 60 mm and 40 mm respectively. Next, this SPA

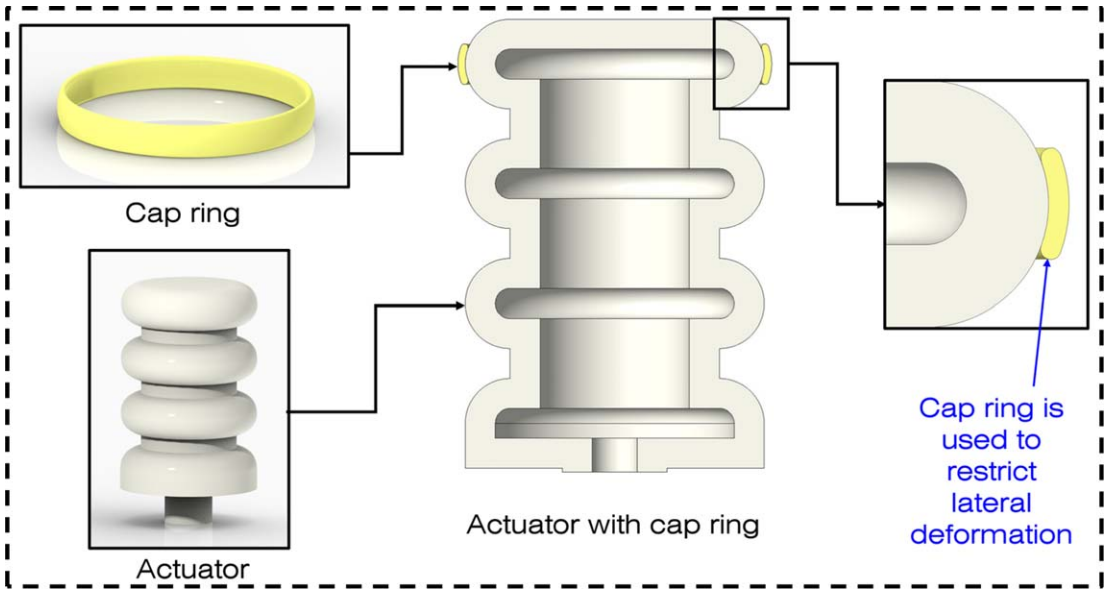

Figure 4. Concept of implementation of cap ring reinforcement.

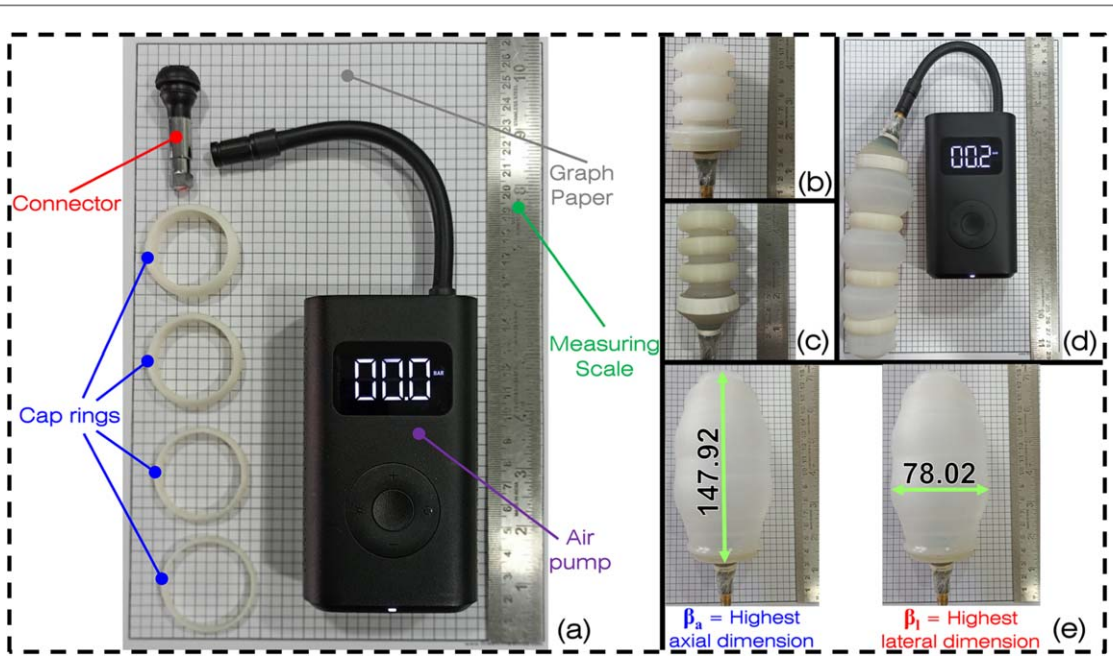

Figure 5. Experimental setup (All dimensions are in mm).

without any cap ring is inflated up to 0.2 bar (20 kPa) pressure using air pump. The axial (β_a) and lateral (β_l) dimensions after inflation are measured and recorded. Then the SPA is deflated by releasing the air pressure. Once the SPA is back to its initial deflated state with original dimensions, then the cap ring configurations are prepared subsequently in the sequence shown in table 2 for one size of cap rings. Each time the post-inflation image is captured and the dimensions are measured using an open online tool [51]. The process is repeated for all sizes of cap rings and measurements are recorded. Here, the major focus is to know the effective change in axial deformation of SPA on the application of cap ring reinforcement at every combination of places on SPA. For that, axial deformation (ε_a) and lateral deformation (ε_l) is calculated for each configuration and listed in table 3.

$\varepsilon_a = \beta_a - \alpha_a =$ Axial deformation, mm;

$\varepsilon_l = \beta_l - \alpha_l =$ Lateral deformation, mm;

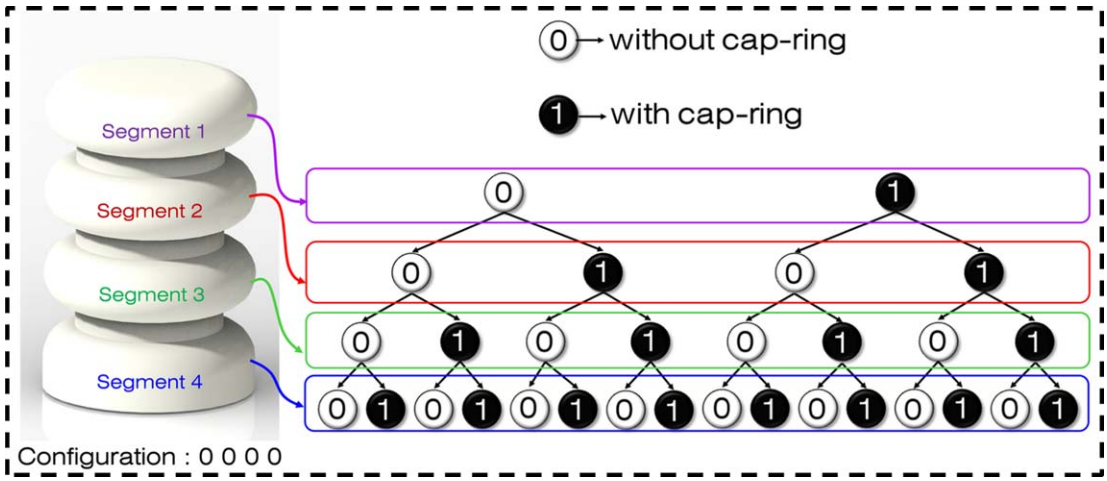

Figure 6. Configuration's labelling illustration.

Table 2. Number of configurations for SPA with 4 segments.

Sr No.	Number of cap rings	Configuration (C)			
1	0	0	0	0	0
2	1	1	0	0	0
3	1	0	1	0	0
4	1	0	0	1	0
5	1	0	0	0	1
6	2	1	1	0	0
7	2	1	0	1	0
8	2	1	0	0	1
9	2	0	1	1	0
10	2	0	1	0	1
11	2	0	0	1	1
12	3	1	1	1	0
13	3	1	1	0	1
14	3	1	0	1	1
15	3	0	1	1	1
16	4	1	1	1	1

The ratio of axial deformation (ε_a) to lateral deformation (ε_l),

$$\lambda = \frac{\text{Axial deformation}}{\text{Lateral deformation}} = \frac{\varepsilon_a}{\varepsilon_l}, \quad (\text{where } \varepsilon_l > 1),$$

represent the effective axial deformation of SPA and hence it is the significant parameter to study the effect of cap ring reinforcement. It is obvious to understand that the higher value of λ represent the more axial deformation per lateral deformation. Hence the objective of the present study is to find the cap ring configuration that provides the highest λ value.

3. Results and discussion

As explained in the preceding section, a comprehensive set of 64 experiments was conducted on a single SPA, incorporating diverse configurations of cap ring reinforcement. The purpose was to assess the impact of reinforcement on effective axial deformation. The outcomes are presented in figure 7, showcasing the post-inflation conditions of various SPA configurations subjected to a pressure of 20 kPa. Evidently, the presence of cap ring reinforcement prominently constrains lateral deformation. A noticeable trend emerges: segments lacking cap ring reinforcement exhibit greater inflation compared to those with cap rings. This observation underscores the effectiveness of cap rings as a means of reinforcement in mitigating lateral deformation.

Table 3. Experimental observations for SPA with different configurations.

Sr No	C	β_a (mm)	β_l (mm)	ε_a (mm)	ε_l (mm)	λ	Sr No	C	β_a (mm)	β_l (mm)	ε_a (mm)	ε_l (mm)	λ
1	40/0000	147.92	78.02	87.92	38.02	2.31	33	80/0000	147.92	78.02	87.92	38.02	2.31
2	40/1000	164.12	87.56	104.12	47.56	2.19	34	80/1000	165.25	82.38	105.25	42.38	2.48
3	40/0100	177.12	91.89	117.12	51.89	2.26	35	80/0100	178.73	88.56	118.73	48.56	2.45
4	40/0010	171.35	84.94	111.35	44.94	2.48	36	80/0010	173.18	81.23	113.18	41.23	2.75
5	40/0001	166.01	86.18	106.01	46.18	2.30	37	80/0001	167.77	84.37	107.77	44.37	2.43
6	40/1100	166.24	86.36	106.24	46.36	2.29	38	80/1100	170.17	83.34	110.17	43.34	2.54
7	40/1010	174.49	85.34	114.49	45.34	2.53	39	80/1010	176.87	82.75	116.87	42.75	2.73
8	40/1001	159.47	84.74	99.47	44.74	2.22	40	80/1001	165.06	83.89	105.06	43.89	2.39
9	40/0110	176.95	72.91	116.95	32.91	3.55	41	80/0110	180.47	72.78	120.47	32.78	3.68
10	40/0101	174.27	90.2	114.27	50.2	2.28	42	80/0101	177.39	86.24	117.39	46.24	2.54
11	40/0011	156.64	83.89	96.64	43.89	2.20	43	80/0011	170.01	81.28	110.01	41.28	2.66
12	40/1110	187.57	77.28	127.57	37.28	3.42	44	80/1110	189.57	70.23	129.57	30.23	4.29
13	40/1101	167.23	81.53	107.23	41.53	2.58	45	80/1101	175.67	80.23	115.67	40.23	2.88
14	40/1011	166.8	83.5	106.8	43.5	2.46	46	80/1011	170.87	82.12	110.87	42.12	2.63
15	40/0111	174.81	71.25	114.81	31.25	3.67	47	80/0111	178.12	69.16	118.12	29.16	4.05
16	40/1111	188.44	67.57	128.44	27.57	4.66	48	80/1111	195.27	65.69	135.27	25.69	5.27
17	60/0000	147.92	78.02	87.92	38.02	2.31	49	100/0000	147.92	78.02	87.92	38.02	2.31
18	60/1000	164.91	87.33	104.91	47.33	2.22	50	100/1000	165.78	80.52	105.78	40.52	2.61
19	60/0100	177.63	89.25	117.63	49.25	2.39	51	100/0100	179.08	87.4	119.08	47.4	2.51
20	60/0010	172.33	83.67	112.33	43.67	2.57	52	100/0010	173.70	79.86	113.7	39.86	2.85
21	60/0001	166.46	85.45	106.46	45.45	2.34	53	100/0001	168.15	84.05	108.15	44.05	2.46
22	60/1100	168.49	85.67	108.49	45.67	2.38	54	100/1100	173.58	82.36	113.58	42.36	2.68
23	60/1010	175.62	83.93	115.62	43.93	2.63	55	100/1010	179.42	80.32	119.42	40.32	2.96
24	60/1001	161.59	84.55	101.59	44.55	2.28	56	100/1001	168.25	82.82	108.25	42.82	2.53
25	60/0110	178.13	72.82	118.13	32.82	3.60	57	100/0110	183.37	70.71	123.37	30.71	4.02
26	60/0101	175.47	87.37	115.47	47.37	2.44	58	100/0101	180.73	81.36	120.73	41.36	2.92
27	60/0011	167.04	82.69	107.04	42.69	2.51	59	100/0011	175.81	81.16	115.81	41.16	2.81
28	60/1110	188.90	72.98	128.9	32.98	3.91	60	100/1110	191.23	66.07	131.23	26.07	5.03
29	60/1101	174.25	81.18	114.25	41.18	2.77	61	100/1101	180.03	79.82	120.03	39.82	3.01
30	60/1011	169.63	83.04	109.63	43.04	2.55	62	100/1011	174.00	80.51	114	40.51	2.81
31	60/0111	176.91	70.18	116.91	30.18	3.87	63	100/0111	186.78	69.08	126.78	29.08	4.36
32	60/1111	192.01	66.8	132.01	26.8	4.93	64	100/1111	202.32	62.87	142.32	22.87	6.22

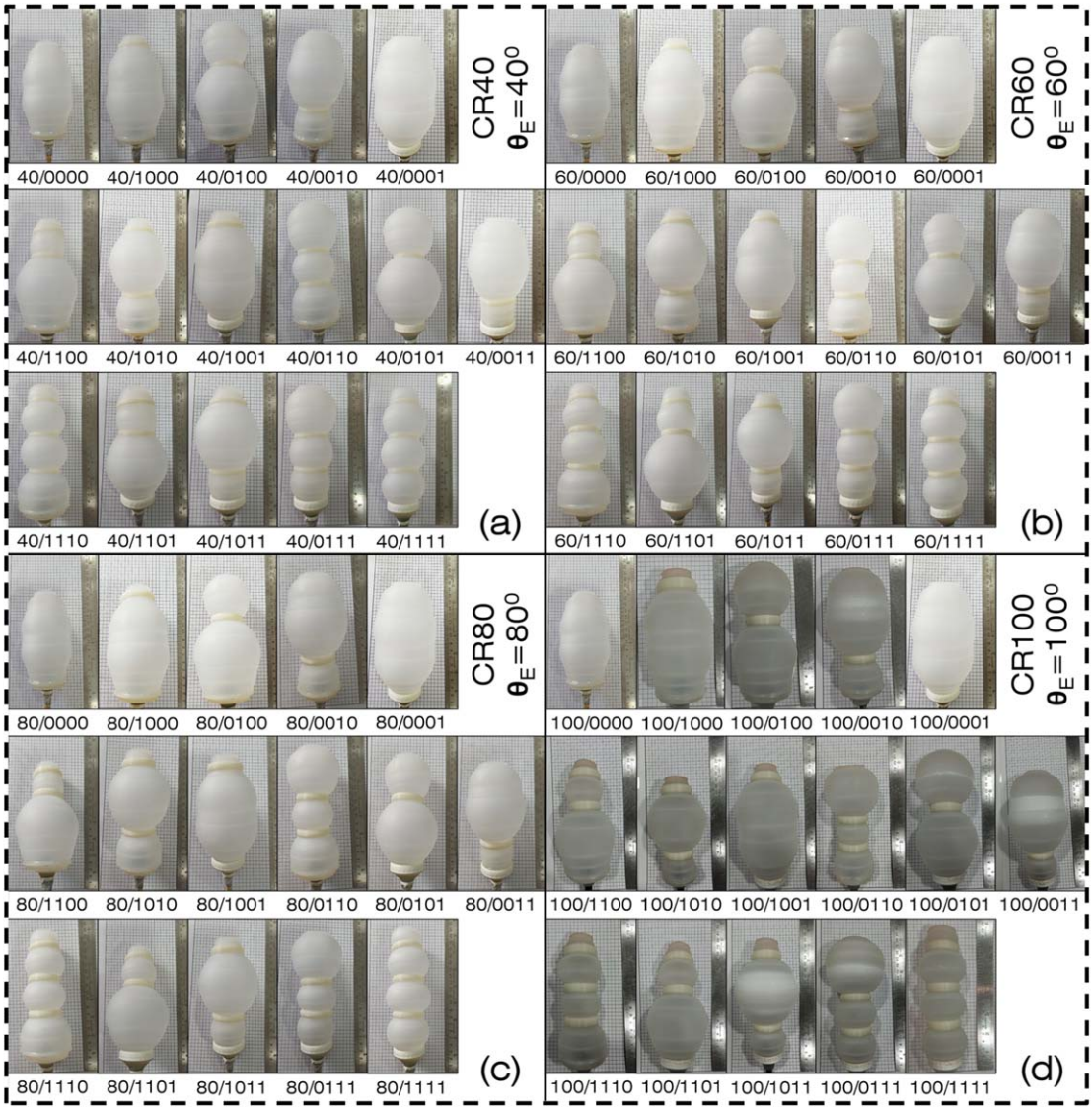

Figure 7. Inflated SPA of different configuration.

3.1. Effect of cap ring geometry

Figures 7(a) through (d) respectively depict inflated SPAs reinforced with cap rings of varying effective arc angles: 40°, 60°, 80°, and 100°. Each top row in figures 7(a)–(d) illustrates an inflated SPA with a single cap ring positioned at different locations. Similarly, the second and third rows portray inflated SPAs with two and three cap rings, respectively. Notably, the leftmost image in each top row represents an inflated SPA devoid of cap rings, while the rightmost image in each third row depicts an inflated SPA featuring four cap rings. The impact of cap ring placement on reinforcement against lateral deformation is clearly evident from figure 7. However, it is worth noting that the positioning of the cap ring also influences axial deformation.

Detailed dimensions of the inflated SPA, including β_a and β_l, alongside axial (ε_a) and lateral (ε_l) deformation, as well as the deformation ratio (λ), are presented in table 3. Interestingly, the λ value for the SPA without a cap ring is recorded at 2.31, serving as the baseline for comparison. Within table 3, not all instances of cap ring configurations yield λ values higher than this baseline of 2.31. This observation highlights that the advantageous effect of cap ring placement is not universally applicable across all configurations. The specific dimensions of the cap ring, their number, and the attachment location all contribute to significant variations in the resulting λ values.

Figure 8 illustrates the relationship between axial deformation, lateral deformation, and the λ ratio across various effective arc angles (θ_E) of cap rings. The results highlight distinct behaviour among different cap ring types. Specifically, when comparing cap rings, CR40 exhibits the least axial deformation and the greatest lateral deformation across all configurations, resulting in the lowest λ value. Conversely, CR100 displays the highest axial deformation and the lowest lateral deformation in each configuration, leading to the highest λ value.

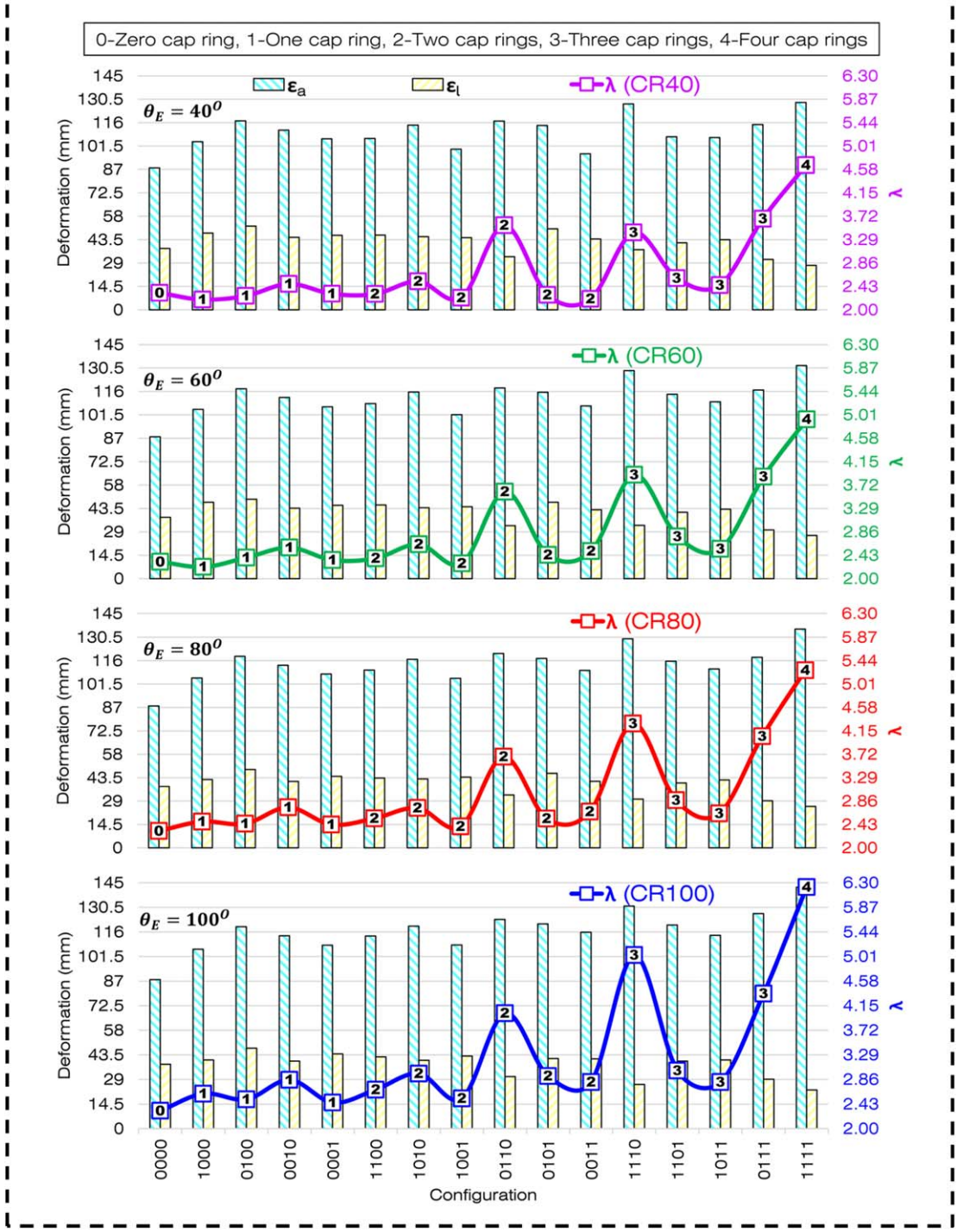

Figure 8. Effect of configurations and effective arc angle.

Furthermore, a consistent pattern emerges: as the effective arc angle of the cap ring increases, so does the λ value. This trend remains consistent across all cases examined.

3.2. Effect of cap ring locations

Besides the effective arc angle of the cap ring, the positioning of the cap ring also has a substantial impact on the axial deformation of the SPA (as demonstrated in figure 9). In a scenario involving a single cap ring (figures 9(a)–(c)), the greatest axial deformation (ε_a) occurs when the cap ring is situated at the second top segment, specifically configuration 0100 (see figure 9(a)). However, this same configuration results in the highest lateral deformation (ε_l) as well (refer to figure 9(b)), leading to a comparatively lower effective deformation ratio λ (depicted in figure 9(c)) compared to other configurations with a single cap ring. The configuration with the highest λ ratio is identified as 0010, where the cap ring is attached to the third top segment. In the scenario of two cap rings, the configuration

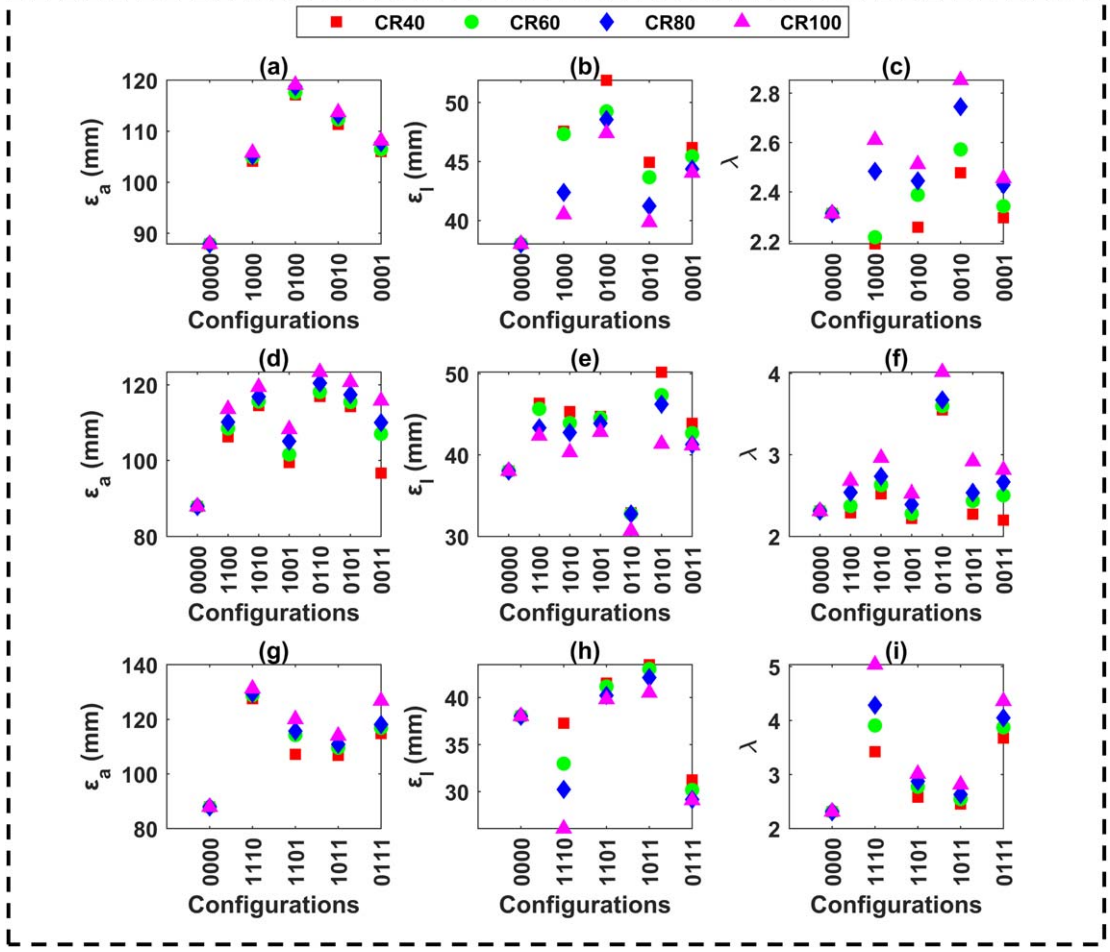

Figure 9. Effect of cap ring locations (a) ε_a with one cap ring, (b) ε_l with one cap ring, (c) λ for one cap ring, (d) ε_a with two cap rings, (e) ε_l with two cap rings, (f) λ for two cap rings, (g) ε_a with three cap rings, (h) ε_l with three cap rings, (i) λ for three cap rings.

yielding the highest axial deformation (ε_a) is 0110 (as shown in figure 9(d)), involving the attachment of cap rings to both middle segments. Interestingly, this configuration displays the least lateral deformation (ε_l) (refer to figure 9(e)), consequently resulting in the highest λ value, as illustrated in figure 9(f). Similarly, for the three-cap ring configuration (figures 9(g)–(i)), the maximum λ value is observed with the 1110 configuration, where two middle segments, along with one top segment, are reinforced with cap rings. Considering all the cases, it becomes evident that the third segment from the top holds significant importance, as reinforcing this segment enhances the λ value, particularly when the upper segments are also reinforced in instances involving more than one cap ring.

3.3. Effect of number of cap ring

Figures 10(a) through (c) exhibit the axial deformation, lateral deformation, and λ ratio for varying configurations with an increasing number of cap rings, progressing from top to bottom. Conversely, figures 10(d) through (f) illustrate the same trends, but with the number of cap rings increasing from bottom to top. Notably, it is observable that augmenting the count of cap rings enhances the λ value, contingent on the positioning of previously reinforced cap rings. However, the sequence in which the cap ring reinforcement is applied also holds significant influence. A comparison between figures 10(c) and (f) highlights this point. In the case of a CR100 cap ring, the 1000 configuration proves more effective than 0001 since it yields a higher λ value when dealing with a solitary cap ring. Similarly, for scenarios involving two cap rings, the 0011 configuration surpasses the 1100 configuration concerning a higher λ value. This distinction arises due to the presence of reinforcement at the third segment, which has been identified as the most crucial segment. For the situation involving three CR100 rings, the 1110 configuration prevails over the 0111 configuration. However, the most notable outcome is achieved with the reinforcement of four cap rings, which yields the optimal results and highest λ value across all cap ring sizes.

The configuration involving the reinforcement of four cap rings, denoted as 1111, stands out as the most effective among all configurations in terms of achieving the highest deformation ratio for cap rings of various sizes. Illustrated in figures 11(a) through (d), this configuration showcases the considerable enhancement in

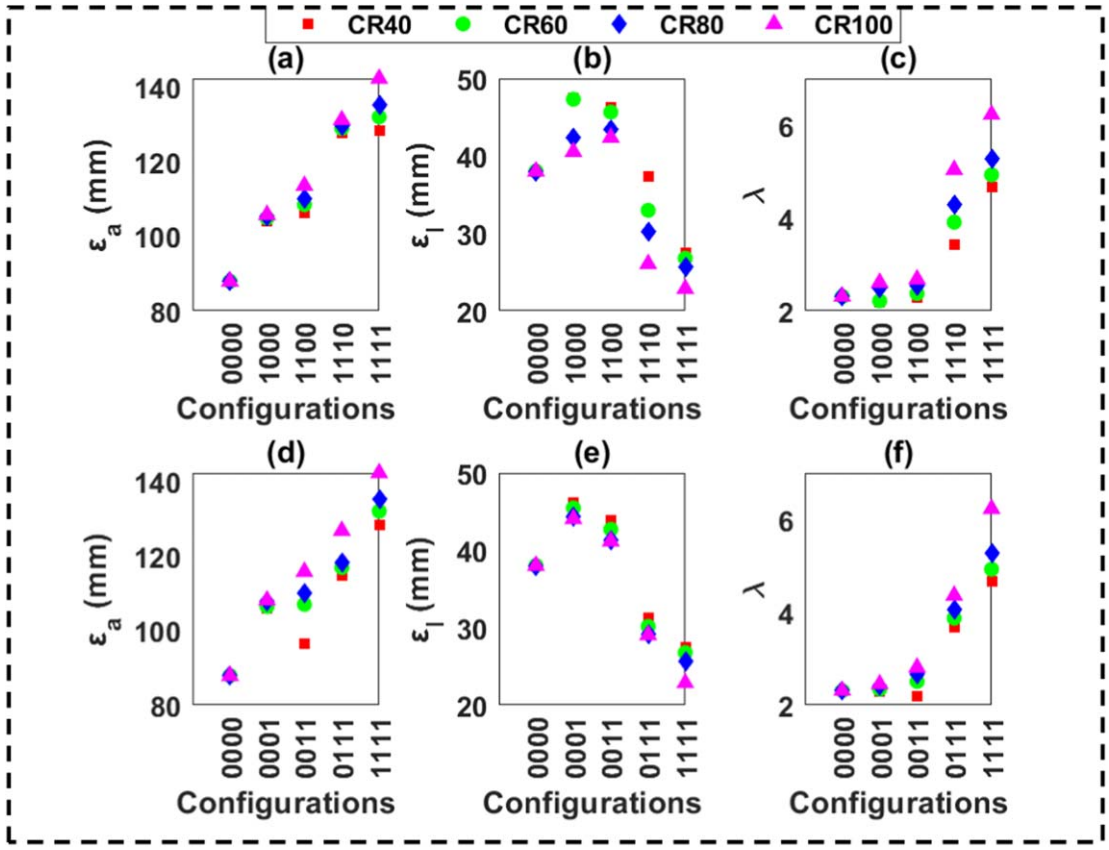

Figure 10. Effect of number of cap rings (a) ε_a, (b) ε_l and (c) λ for increasing cap rings from top to bottom; (d) ε_a, (e) ε_l and (f) λ for increasing cap rings from bottom to top.

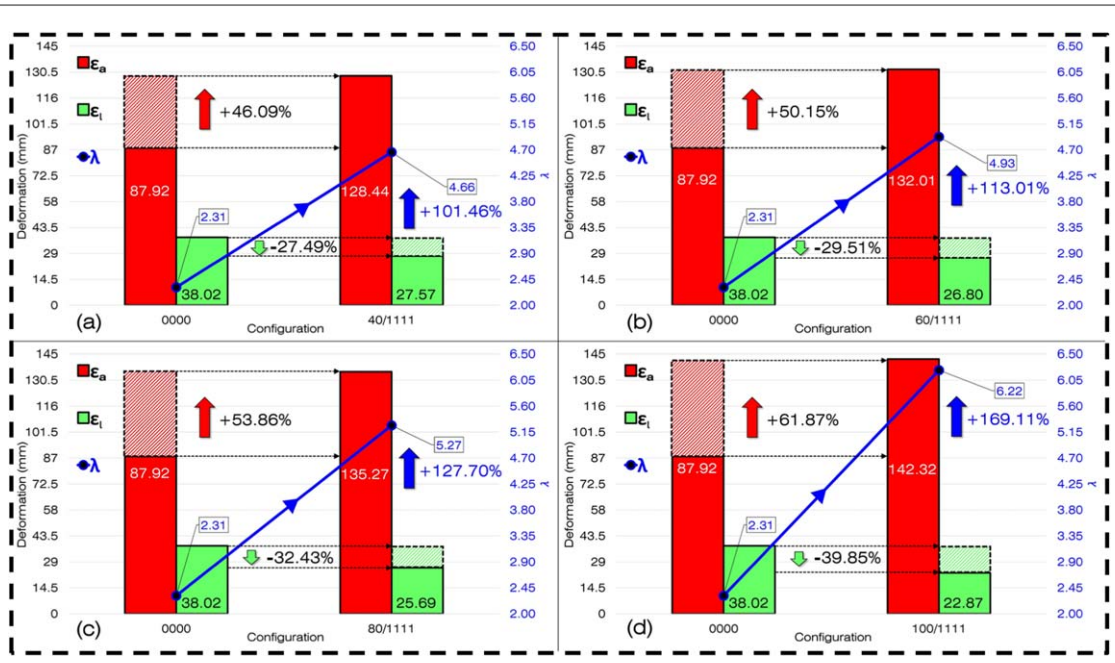

Figure 11. Overall %gain in pure axial deformation (λ), (a) CR40, (b) CR60, (c) CR80, (d) CR100.

pure axial deformation when compared to the scenario with no cap rings, for four different cap ring sizes: CR40, CR60, CR80, and CR100. When all four rings of CR40 size are incorporated, the axial deformation experiences a notable increase of 46.09%, accompanied by a reduction of 27.49% in lateral deformation. This combination results in an impressive overall gain of 101.46% in pure axial deformation. Similarly, for CR60 cap rings, the

axial deformation escalates by 50.15%, complemented by a decrease of 29.51% in lateral deformation. This leads to a remarkable overall gain of 113.01% in pure axial deformation. The reinforcement of CR80 cap rings yields a substantial 53.86% increment in axial deformation, coupled with a reduction of 32.43% in lateral deformation. This results in a substantial overall gain of 127.70% in pure axial deformation. Following a similar pattern, the CR100 cap ring reinforcement leads to a remarkable 61.87% increase in axial deformation, while concurrently reducing lateral deformation by 39.85%. This outstanding performance culminates in an impressive overall improvement of 169.11% in pure axial deformation. Evidently, the configuration employing CR100 cap rings with the 1111 arrangement emerges as the most superior among all the experimented configurations. It offers the most significant enhancement in pure axial deformation, underlining its effectiveness in maximizing deformation ratios for the given cap ring sizes.

4. Conclusion

This study investigates the impact of cap ring reinforcement on the deformation of LSR-based SPAs with a shore hardness of 15A. Cap ring reinforcement emerges as a cost-effective and easily implementable solution. To comprehensively analyse its effects, 64 distinct configuration cases were meticulously tested. These configurations encompassed a range of factors, including the number of rings (ranging from 0 to 4), ring placement (across 4 different locations), and variations in ring size. The results underscore the noteworthy reduction in lateral deformation brought about by cap ring reinforcement, highlighting its advantageous nature. However, the investigation also revealed that the specific arrangement and count of cap rings play pivotal roles in achieving optimal customized outcomes. One key conclusion drawn is that augmenting the count of cap rings corresponds to an increase in pure axial deformation, quantified by the λ ratio. Notably, the segment positioned third from the top is of paramount importance for effective reinforcement, particularly when other upper segments are similarly reinforced in cases involving multiple rings. However, the equal size of reinforcement to all the four segments results the maximum pure axial deformation out of all experimented configuration

Additionally, the study observes a correlation between the cap ring's effective arc angle and the λ ratio. Notably, the CR100 cap ring demonstrates the highest λ ratio among all tested sizes. This experimental exploration underscores the advantageous nature of cap ring reinforcement for enhancing pure axial deformation in SPAs, provided it is applied at the appropriate location, with a suitable arc angle, and in an optimal number. Furthermore, the cost-effectiveness of cap ring manufacturing and its straightforward implementation requiring no additional adhesive adds to its appeal. The proposed SPA with cap ring reinforcement is a versatile innovation which can be used in certain applications wherein axial deformation or linear motion of SPA are desired for example, prosthetic limbs, surgical tools, harvesting and plant care, rehabilitation devices, etc This study lays the groundwork for further extensions, such as investigating diverse cap ring designs, optimizing the cap ring's arc angle for maximal pure axial deformation, varying the SPA's shape to further enhance performance, and exploring alternative reinforcement techniques for even greater deformation.

Data availability statement

The data cannot be made publicly available upon publication because no suitable repository exists for hosting data in this field of study. The data that support the findings of this study are available upon reasonable request from the authors.

Funding

This research was supported by Nirma University under the scheme of Minor Research Project grant award #IT/2022–23/06. This research was also supported in part by National Science Foundation award #2205205 and the National Institute of Biomedical Engineering and Bioengineering of the National Institutes of Health award number R01EB025819.

ORCID iDs

Vishal Mehta https://orcid.org/0000-0001-5947-1390
Mihir Chauhan https://orcid.org/0000-0002-0145-9273
Erik D Engeberg https://orcid.org/0000-0002-2340-1881

References

[1] Kim J, Kim J W, Kim H C, Zhai L, Ko H U and Muthoka R M 2019 Review of soft actuator materials *Int. J. Precis. Eng. Manuf.* **20** 2221–41

[2] Asaka K and Okuzaki H 2014 Progress and Current Status of Materials and Properties of Soft Actuators *Soft Actuators: Materials, Modeling, Applications, and Future Perspectives* (Springer) 3–18

[3] Walker J, Zidek T, Harbel C, Yoon S, Strickland F S, Kumar S and Shin M 2020 Soft robotics: a review of recent developments of pneumatic soft actuators *Actuators* **9** 3

[4] Lin M, Paul R, Abd M, Jones J, Dieujuste D, Chim H and Engeberg E D 2023 Feeling the beat: a smart hand exoskeleton for learning to play musical instruments *Front Robot AI* **10** 1212768

[5] Zhao S, Wang Z, Lei Y, Zhang J, Li Y, Sun Z and Gong Z 2022 3D-printed soft pneumatic robotic digit based on parametric kinematic model for finger action mimicking *Polymers* **14** 2786

[6] Sun Y, Zhang Q and Chen X 2020 Design and analysis of a flexible robotic hand with soft fingers and a changeable palm *Adv. Robot.* **34** 1041–54

[7] Salem M E M, Wang Q, Wen R and Xiang M 2018 Design and characterization of soft pneumatic actuator for universal robot gripper *2018 Int. Conf. on Control and Robots* 2018 (ICCR) 6–10

[8] Li M, Zhuo Y, Chen J, He B, Xu G, Xie J, Zhao X and Yao W 2020 Design and performance characterization of a soft robot hand with fingertip haptic feedback for teleoperation *Adv. Robot.* **34** 1491–505

[9] Lee S, Kwon S, Kim Y and Lee K 2016 A method of vertical and horizontal force estimation by using air-filled material and camera for soft physical human-robot interaction: fundamental experiments *Adv. Robot.* **30** 352–9

[10] Laschi C, Cianchetti M, Mazzolai B, Margheri L, Follador M and Dario P 2012 Soft robot arm inspired by the octopus *Adv. Robot.* **26** 709–27

[11] Hao L, Xiang C, Giannaccini M E, Cheng H, Zhang Y, Nefti-Meziani S and Davis S 2018 Design and control of a novel variable stiffness soft arm *Adv. Robot.* **32** 605–22

[12] Ito K, Homma Y and Rossiter J 2020 The soft multi-legged robot inspired by octopus: climbing various columnar objects *Adv. Robot.* **34** 1096–109

[13] Zhang J, Zhou J, Yuan S and Jing C 2019 Design, fabrication and experiments of a 3D-motion soft elastomer actuator *Proc. of 2019 IEEE Int. Conf. on Mechatronics and Automation* 2019 (ICMA) 497–501

[14] Youssef S M, Soliman M, Saleh M A, Mousa M A, Elsamanty M and Radwan A G 2022 Modeling of soft pneumatic actuators with different orientation angles using echo state networks for irregular time series data *Micromachines* **13** 216

[15] Nishikawa Y and Matsumoto M 2019 A design of fully soft robot actuated by gas–liquid phase change *Adv. Robot.* **33** 567–75

[16] Mehta V and Chauhan M 2021 Effect of geometrical shape on axial deformation of soft actuator *Journal of Physics: Conf. Series* 2115 (IOP Publishing Ltd)

[17] Mehta V and Chauhan M 2024 Conceptualization and topology optimization of ampheel: an integration of rolling wheel and turtle-inspired mechanism for amphibious mobile robot *International Journal of Robotics and Control Systems* **4** 334–53

[18] Hayakawa Y, Kida K, Nakanishi Y, Ichii H and Hirota Y 2022 Development and application of silicone outer shell-type pneumatic soft actuators *Journal of Robotics and Mechatronics* **34** 444–53

[19] Guo J, Low J H, Liu J, Li Y, Liu Z and Yeow C H 2022 Three-dimensional printable ball joints with variable stiffness for robotic applications based on soft pneumatic elastomer actuators *Polymers* **14** 3542

[20] Du T, Sun L and Wan J 2022 A worm-like crawling soft robot with pneumatic actuators based on selective laser sintering of TPU powder *Biomimetics* **7** 205

[21] Connolly F, Walsh C J and Bertoldi K 2017 Automatic design of fiber-reinforced soft actuators for trajectory matching *Proc. Natl. Acad. Sci. U S A* **114** 51–6

[22] V V, S S and A R V 2022 Optimization of elephant trunk soft pneumatic actuator using finite element method *World Journal of Engineering* **19** 832–42

[23] Doreswamy D, B R A, D'Souza J M, H K S and Bhat S K 2023 Numerical investigation on the effect of pressurization scenarios on the deformation behaviours and operating volume of a four-chambered soft actuator *World Journal of Engineering* **21** 709–19

[24] Bousbia L, Amouri A and Cherfia A 2023 Dynamics modeling of a 2-DoFs cable-driven continuum robot *World Journal of Engineering* **20** 631–40

[25] Venkatesan V, Shanmugam S and Veerappan A.R. 2022 Structural analysis of bending soft pneumatic network actuators for various designs using the finite element method *World Journal of Engineering* **20** 1088–96

[26] Sayyadan S M Z and Moniri M M 2021 A bio-inspired soft planar actuator capable of broadening its working area *Eng. Res. Express* **3** 025029

[27] Salem M E M and Wang Q 2022 Dimension investigation to pneumatic network bending soft actuators for soft robotic applications *Eng. Res. Express* **4** 015001

[28] Sutton L and Menon C 2019 Soft fluidic actuator based on nylon artificial muscles *Eng. Res. Express* **1** 015012

[29] Jung J C, Jang J H and Rodrigue H 2019 Inflatable L-shaped prisms as soft actuators for soft exogloves *Eng. Res. Express* **1** 025009

[30] Morishima M, Umedachi T and Kawahara Y 2020 Caterpillar-inspired soft robot that locomotes upside-down by utilizing environmental skeleton *Eng. Res. Express* **2** 035022

[31] Wang T, Wang X, Fu G and Lu C 2023 Passively stretchable vacuum-powered artificial muscle with variable stiffness skin *Eng. Res. Express* **5** 045028

[32] Farmer C and Medina H 2020 Dimensionless parameter-based numerical model for double conical dielectric elastomer actuators *Eng. Res. Express* **2** 035020

[33] Ovy S M A I, Stano G, Percoco G, Cianchetti M and Tadesse Y 2023 Inexpensive monolithic additive manufacturing of silicone structures for bio-inspired soft robotic systems *Eng. Res. Express* **5** 015016

[34] Hernandez-Barraza L, Kalil-Khan A and Yeow R C H 2023 A bioinspired modular soft robotic arm *Eng. Res. Express* **5** 015021

[35] Rodriguez S, Galvan R and Ganta D 2021 Modelling and simulation of soft robotic human tongue with improved motion *Eng. Res. Express* **3** 045027

[36] Su H, Hou X, Zhang X, Qi W, Cai S, Xiong X and Guo J 2022 Pneumatic soft robots: challenges and benefits *Actuators* **11** 92

[37] Zhu Y, Feng K, Hua C, Wang X, Hu Z, Wang H and Su H 2022 Model analysis and experimental investigation of soft pneumatic manipulator for fruit grasping *Sensors* **22** 4532

[38] Baranwal A and Agnihotri P K 2022 Harnessing fiber induced anisotropy in design and fabrication of soft actuator with simultaneous bending and twisting actuations *Compos. Sci. Technol.* **230** 109724

[39] Fras J and Althoefer K 2019 Soft fiber-reinforced pneumatic actuator design and fabrication: towards robust, soft robotic systems *Lecture Notes in Computer Science* 11649 (Springer) (https://doi.org/10.1007/978-3-030-23807-0_9)
[40] Gariya N, Kumar P and Singh T 2023 Experimental study on a bending type soft pneumatic actuator for minimizing the ballooning using chamber-reinforcement *Heliyon* **9** e14898
[41] Ma K, Jiang Z, Gao S, Cao X and Xu F 2022 Design and analysis of fiber-reinforced soft actuators for wearable hand rehabilitation device *IEEE Robot Autom Lett* **7** 6115–22
[42] Moss A, Krieg M and Mohseni K 2021 Modeling and characterizing a fiber-reinforced dielectric elastomer tension actuator *IEEE Robot Autom Lett* **6** 1264–71
[43] Nguyen P H, Sridar S, Zhang W and Polygerinos P 2017 Design and control of a 3-chambered fiber reinforced soft actuator with off-the-shelf stretch sensors *Int. J. Intell. Robot Appl.* **1** 342–51
[44] Rakhtala S M and Ghayebi R 2022 Real time control and fabrication of a soft robotic glove by two parallel sensors with MBD approach *Med. Eng. Phys.* **100** 103743
[45] Singh G and Krishnan G 2020 Designing fiber-reinforced soft actuators for planar curvilinear shape matching *Soft Robot* **7** 109–21
[46] Singh G, Xiao C, Hsiao-Wecksler E T and Krishnan G 2018 Design and analysis of coiled fiber reinforced soft pneumatic actuator *Bioinspir Biomim* **13** 036010
[47] Chen Z, Zou A, Qin Z, Han X, Li T and Liu S 2021 Modeling and fabrication of soft actuators based on fiber-reinforced elastomeric enclosures *Actuators* **10** 127
[48] Wei Q, Xu H, Sun F, Chang F, Chen S and Zhang X 2022 Biomimetic fiber reinforced dual-mode actuator for soft robots *Sens. Actuators* A **344** 113761
[49] Xu M, Wang G and Rong C 2022 Fiber-reinforced flexible joint actuator for soft arthropod robots *Sens. Actuators* A **340** 113522
[50] Chemzest 2022 Liquid silicone rubber available at https://chemzest.com/liquid-silicone-rubber/ (accessed 15 August 2022)
[51] Anon 2023 Photo measure *Eleif* available at https://eleif.net/photomeasure# (accessed 24 March 2023)